nature communications

Article

https://doi.org/10.1038/s41467-026-69109-5

Fluorescence mapping of atropisomer populations enabled by through-space conjugation

Received: 15 October 2025

Accepted: 26 January 2026

Published online: 31 January 2026

Check for updates

Qingyang Xu[1,2,3,8], Kangwei Luo[1,2,3,8], Yipu Wang[4,8], Jiajie Wu[1,2,3], Hongwei Lu[1,2,3], Manyu Chen[1,2,3], Zuping Xiong[1,2,3], Jing Zhi Sun[1], Jianyu Zhang[1,5] ✉, Feihe Huang[2,6] ✉, Ben Zhong Tang[7] ✉ & Haoke Zhang[1,2,3] ✉

Multi-axis atropisomers are ubiquitous in nature, and their intricate stereoconformations not only deepen stereochemical understanding but also elucidate fundamental principles of molecular atropisomeric dynamics. Nevertheless, insights into multi-axis atropisomerism remain limited. This work presents a systematic investigation of three classes of LaPlente-type biaxial atropisomers based on naphthalene rotors and phenyl linkers. Thermodynamically and kinetically controlled interconversion of molecular conformations is achieved in 22-NB, 11-NB, and 11-NB-8DMe. Concurrently, a direct correlation between molecular dynamics and electronic through-space conjugation (TSC) is elucidated. Furthermore, absolute separation of *syn* and *anti* conformers is accomplished in 11-NB-2DMe, whose distinct TSC-induced fluorescence enables direct visualization of dynamic conformer populations and kinetics during temporally sequential crystallization. This work provides fundamental mechanistic insights into multi-axis atropisomer stereochemistry and establishes a fluorescence-based approach as an in-situ platform for real-time analysis of molecular dynamics across life and materials sciences.

Atropisomers, a class of stereoisomers arising from restricted single-bond rotation due to steric hindrance, exhibit distinct conformational stability dictated by their rotational energy barriers[1]. These isomers exhibit broad applications across life sciences to advanced materials. For instance, in pharmaceutical science, atropisomers function as targeted enzyme inhibitors by leveraging conformation-selective binding to modulate biological activity, with their stereochemical configuration critically influencing drug efficacy, pharmacokinetics, and bioavailability[2,3]. Similarly, in materials science, atropisomerism underpins the design of chiral molecules[4,5] and artificial molecular motors[6,7], driving asymmetric catalysis and dynamic nanotechnology[8–10]. Despite these advances, current research has predominantly focused on monoaxial atropisomeric frameworks, particularly Type I systems such as biphenyl and binaphthyl derivatives (Fig. 1a)[11,12]. While notable progress has been achieved in monoaxial Type II and III atropisomers[13–18], the study of

[1]MOE Key Laboratory of Macromolecular Synthesis and Functionalization, Department of Polymer Science and Engineering, Zhejiang University, Hangzhou, China. [2]Zhejiang-Israel Joint Laboratory of Self-Assembling Functional Materials, ZJU-Hangzhou Global Scientific and Technological Innovation Center, Zhejiang University, Hangzhou, China. [3]State Key Laboratory of Transvascular Implantation Devices, Hangzhou, China. [4]School of Chemistry and Chemical Engineering, Nantong University, Nantong, China. [5]State Key Laboratory of Biobased Transportation Fuel Technology, Zhejiang University, Hangzhou, China. [6]Stoddart Institute of Molecular Science, Department of Chemistry, Zhejiang University, Hangzhou, China. [7]Guangdong Basic Research Center of Excellence for Aggregate Science, School of Science and Engineering, The Chinese University of Hong Kong, Shenzhen, Guangdong, China. [8]These authors contributed equally: Qingyang Xu, Kangwei Luo, Yipu Wang. ✉e-mail: zhangjianyu@zju.edu.cn; fhuang@zju.edu.cn; tangbenz@cuhk.edu.cn; zhanghaoke@zju.edu.cn

https://doi.org/10.1038/s41467-026-69109-5

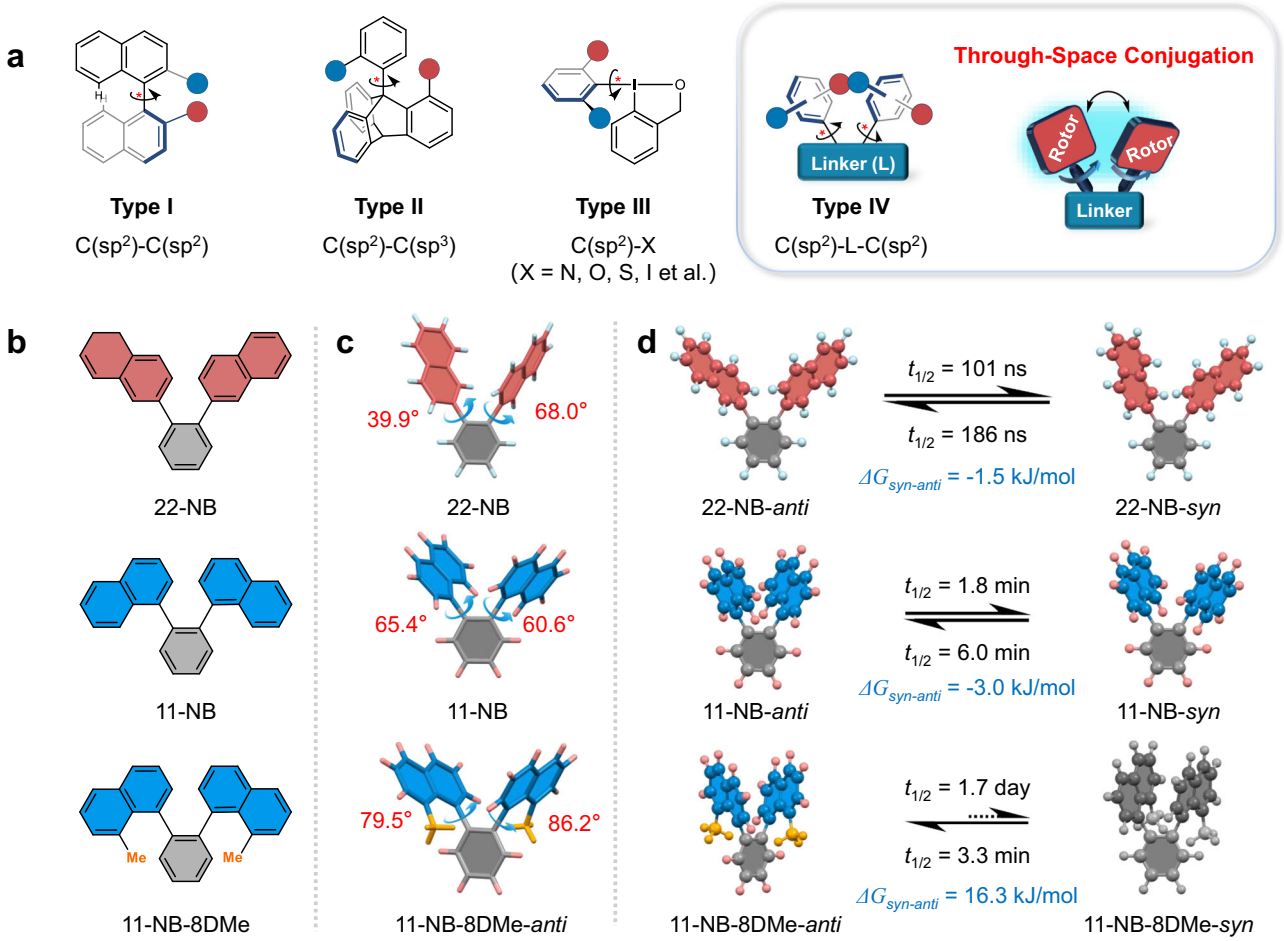

Fig. 1 | Types of atropisomers and thermodynamic/kinetic control. **a** Representative types of atropisomers. **b** Chemical structures of 22-NB, 11-NB, and 11-NB-8DMe. **c** Single-crystal structures and dihedral angles of these atropisomers. **d** Free energy differences (ΔG) between *syn* and *anti* conformers and interconversion half-lives ($t_{1/2}$). **e**, **f** Temperature-dependent NMR and *syn*/*anti* ratios of 11-NB. For clearer visualization, hydrogen atom counts are reduced based on symmetry considerations, where red represents 11-NB-*syn* and blue represents 11-NB-*anti*.

naturally occurring multi-axis atropisomers involving higher-order stereochemical complexity remains in its infancy[10,19,20]. Thus, investigating these systems is essential, as it promises to expand fundamental stereochemical theory and offers insights into the conformational dynamics governing biological and functional materials.

Meanwhile, the structural elucidation of atropisomers typically relies on single-crystal X-ray diffraction (XRD)[21], nuclear magnetic

resonance (NMR) spectroscopy[22], and circular dichroism (CD)[23]. However, these techniques are inherently limited by requirements such as high crystallinity, well-resolved NMR signals, or strong chiroptical activity, which restrict their broader applicability. In contrast, fluorescence-based methods offer ultrasensitivity and versatility to overcome such constraints. Recent studies verify that noncovalent through-space conjugation (TSC) in sterically hindered twisted molecules modulates electronic structures via spatial orbital overlap, generating conformation-dependent fluorescence signals[24–27]. Moreover, leveraging the crowded topology of atropisomers, this TSC-driven fluorescence approach may emerge as a powerful alternative for structural analysis and real-time monitoring of dynamic conformational equilibria.

In this work, a series of biaxial atropisomers (namely, Type IV systems) by integrating two naphthyl rotors with a phenyl-based linker are constructed (Fig. 1a, Supplementary Figs. 1–32 and Supplementary Table 1). Through precise modulation of rotor steric hindrance, three LaPlente-classified atropisomers with different TSC features are obtained[28,29]. Precise control over the thermodynamic and kinetic interconversions of their conformers in 22-NB, 11-NB, and 11-NB-8DMe is also achieved, elucidating the correlation among molecular dynamics, electronic TSC, and fluorescent signals. Notably, complete separation of stable *syn* and *anti* conformers is achieved for 11-NB-2DMe, and its conformer-dependent fluorescence variations induced by TSC successfully enable quantitative analysis for resolving *syn* and *anti* populations in dilute solution. This developed fluorescent spectroscopy approach further realizes real-time visualization of crystallization-driven conformer redistribution, providing high resolution of atropisomer dynamics. Beyond expanding the multidimensional stereochemical framework of atropisomers, this work establishes a versatile in-situ methodology for mapping atropisomeric populations with high precision.

Results

Thermodynamic and kinetic control of atropisomers

The biaxial atropisomers, namely 22-NB and 11-NB, were synthesized, and their chemical structures and purity were confirmed through XRD and high-performance liquid chromatography (HPLC) analyses, respectively (Fig. 1b, c, Supplementary Fig. 30). However, NMR characterization reveals divergent properties between these structurally similar compounds. 22-NB displays a single set of well-resolved signals perfectly matching its expected structure, whereas 11-NB exhibits two distinguishable sets of peaks from its two conformers (Supplementary Figs. 8–11). To investigate the underlying mechanism, potential energy surface scans of the naphthyl rotor and phenyl linker for both 22-NB and 11-NB were performed (Supplementary Figs. 33, 34). The computational analysis reveals striking differences in their rotational profiles: 22-NB displays a relatively flat energy landscape with a maximum rotational barrier of 31.2 kJ/mol, while 11-NB exhibits two well-defined energy minima corresponding to stable *syn* and *anti* conformations, separated by a substantial rotational barrier of 88.2 kJ/mol. This pronounced energy difference provides a quantitative explanation for their distinct NMR characteristics, with a higher barrier of 11-NB enabling the observation of two stable conformers.

Quantitative analysis of the free energy and conformational transition half-life ($t_{1/2}$) of the *syn* and *anti* conformers also reveals differences between these atropisomeric systems. For 22-NB, the calculated $t_{1/2}$ for *syn* and *anti* interconversion are short (101 ns for *anti* to *syn* and 186 ns for *syn* to *anti*), which is consistent with its low rotational barrier (Fig. 1d and Supplementary Fig. 38). In contrast, 11-NB exhibits significantly prolonged $t_{1/2}$ of 1.8 min and 6.0 min, demonstrating effective kinetic stability of both conformers. This kinetic disparity indicates that rapid single-bond rotation in 22-NB results in NMR signal averaging, while the slower conformational transition rate in 11-NB enables resolution of two distinct conformers. Furthermore, thermodynamic analysis confirms the *syn* conformation as energetically favored, corresponding to a larger population ratio.

Variable-temperature ^{1}H NMR analysis of 11-NB provides direct evidence of temperature-dependent conformer equilibria. As the temperature decreased from 320 K to 240 K, an increase of the *syn* conformer population from 60.0% to 63.2% was observed (Fig. 1e, f), demonstrating the dynamic equilibrium toward the thermodynamically favored conformation at a low temperature. In contrast, parallel experiments on 22-NB show no observable spectral changes across the same temperature range, consistent with its rapid conformer interconversion (Supplementary Fig. 22). The dynamic interconversion of 11-NB is also realized and validated by its NMR spectra across diverse solvent environments (Supplementary Fig. 23). Expanding the investigation to a higher complexity system, a triaxial atropisomer (namely 111-NB) with three conformers could also be obtained (Supplementary Figs. 12, 13). Critically, this result demonstrates that the conformational equilibrium observed in 11-NB is not an isolated occurrence but rather a generalizable phenomenon.

To further investigate the steric hindrance effect on the biaxial atropisomers, 11-NB-8DMe with two additional methyl groups was subsequently designed. Surprisingly, this derivative exhibits a single stable conformer, contrasting sharply with the dynamic behavior of its parent compound of 11-NB (Fig. 1b, c, Supplementary Figs. 15, 16). Computational analysis of free energy and $t_{1/2}$ provided mechanistic insights into this observation. Although both *syn* and *anti* conformations exist in 11-NB-8DMe, the free energy of the *syn* conformer is 16.3 kJ/mol higher than the *anti* conformer, resulting in the thermodynamically stable *anti* conformer (Fig. 1d, Supplementary Figs. 36, 38). This substantial energy difference originates from severe intramolecular steric hindrance between adjacent methyl groups in the *syn* conformer, while the *anti* conformer remains sterically unencumbered. Moreover, the kinetic barrier leads to more than a 700-fold disparity in interconversion rates, resulting in a rapid transition from *syn* to *anti* ($t_{1/2}$ = 3.3 min) but a slow reverse transition from *anti* to *syn* ($t_{1/2}$ = 1.7 day), effectively quenching the population of the *syn* conformer at equilibrium.

The above thermodynamic and kinetic regulation of atropisomers reveals two essential principles for achieving complete conformer separation in atropisomeric systems: (i) Minimal free energy differences to ensure thermodynamic coexistence without a significant population bias toward either isomer. (ii) Sufficient interconversion barriers to trap the conformers in their respective states, thereby suppressing thermal equilibration over experimentally relevant timescales.

Electronic TSC in atropisomers

The photophysical properties of 22-NB, 11-NB, and 11-NB-8DMe-*anti* were further systematically investigated (Supplementary Figs. 39–49 and Supplementary Table 3). All three atropisomers show the absorption maximum ≤290 nm, a typical feature of isolated naphthalene rings (Supplementary Figs. 39–40). To elucidate whether through-bond conjugation (TBC) or TSC dominates the photoluminescence (PL) process in biaxial atropisomer systems, three model compounds were characterized. As shown in Supplementary Fig. 45a, temperature-dependent PL spectra in dilute 2-methyltetrahydrofuran (2-Me-THF) reveal that naphthalene (Naph) exhibits intrinsic emission at 321/336 nm. The emission of 2-phenylnaphthalene (2-NB) redshifts to 358 nm relative to Naph (Supplementary Fig. 45b), attributable to extended TBC. In contrast, 1-phenylnaphthalene (1-NB) displays a blueshifted emission at 345 nm (Supplementary Fig. 45c). This shift indicates that steric hindrance between naphthalene and benzene rings in 1-NB induces a large dihedral angle, disrupting side-by-side orbital overlap and causing significant blueshift (consistent with our previous finding that twisted conformations disrupt TBC[26]).

https://doi.org/10.1038/s41467-026-69109-5

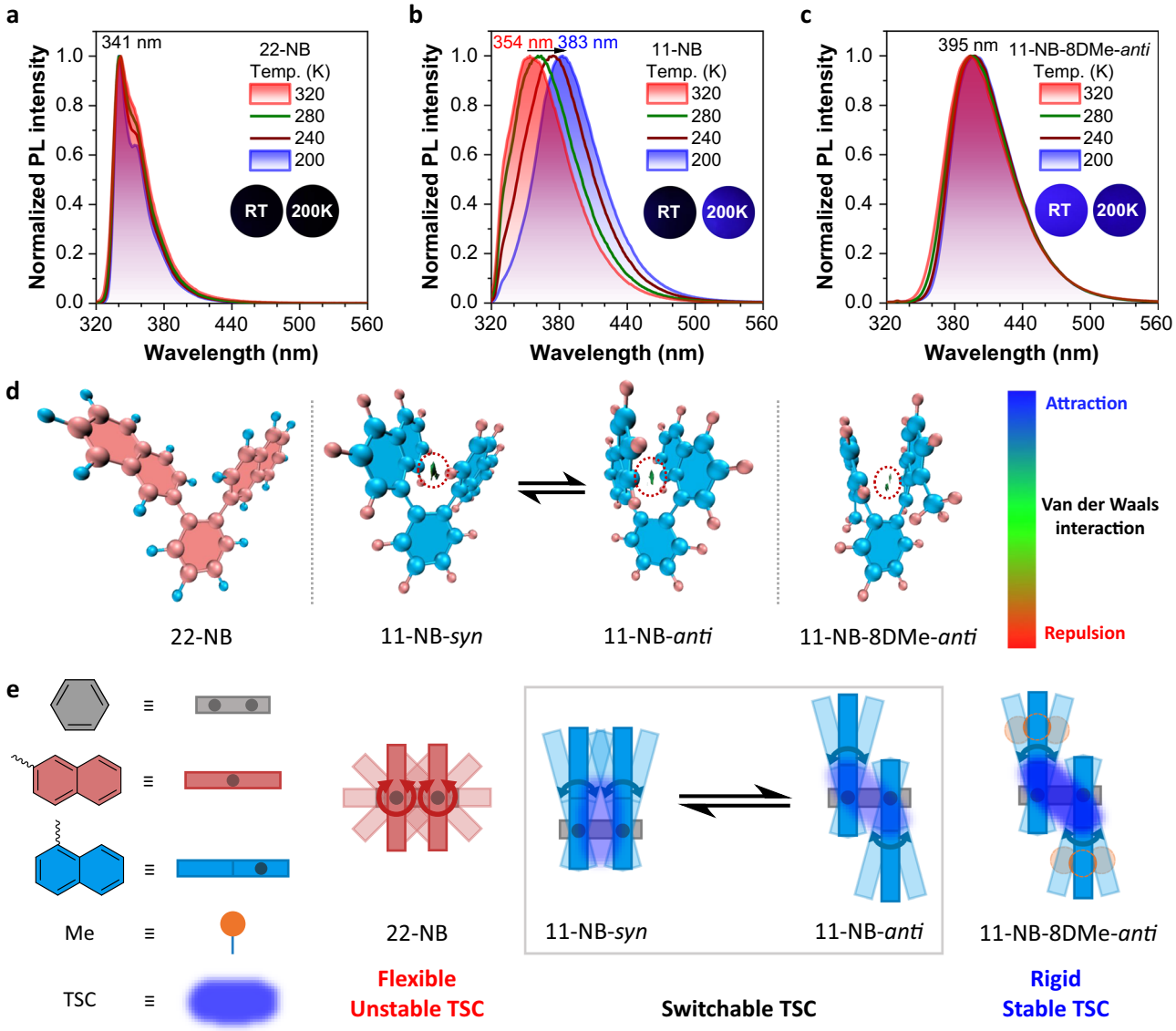

Fig. 2 | Photophysical properties and intramolecular through-space conjugation (TSC). Temperature-dependent photoluminescence (PL) spectra of **a** 22-NB, **b** 11-NB, and **c** 11-NB-8DMe-*anti* in 2-Me-THF, $c = 10$ μM. The inset displays solution photographs captured at room temperature (RT) and 200 K under 300 nm excitation. **d** The excited-state geometries of these three compounds were analyzed using IGMH (isovalue = 0.018 a. u.) to characterize the interactions between the two naphthalene rings, which are highlighted within red-dashed boxes to visualize their specific locations and features. The colors represent the interaction characteristics and intensities on the isosurface around the critical points, as shown in the color scale. **e** The relationship between the flexibility of the molecular skeleton and TSC.

In biaxial atropisomer system, 22-NB exhibits isolated Naph emission at 341 nm (Fig. 2a), showing a blueshift relative to 2-NB (358 nm). This spectral shift indicates that steric hindrance between the naphthalene rings increases their torsion angle relative to the connecting benzene ring, thereby disrupting TBC. Meanwhile, this configuration fails to establish TSC[30]. On the contrary, 11-NB displays an emission peak at 354 nm at 320 K (Fig. 2b), which is redshifted compared to that of 1-NB at 345 nm, suggesting the formation of TSC between two naphthalene fragments linked by the phenyl unit. Furthermore, the emission peak further redshifts to 383 nm with the decreased temperature, indicating the gradual enhancement and stable existence of TSC due to the rigid external environment upon cooling. Compared with most reported systems that require aggregation for TSC stabilization[31], the single-molecule state TSC of 11-NB indicates strong intramolecular steric hindrance that stabilizes the conformation. Meanwhile, 11-NB-8DMe-*anti* displays a temperature-independent emission peak at 395 nm, demonstrating its highly stable and strong TSC (Fig. 2c). Furthermore, the aggregation-dependent PL studies in acetonitrile/water mixtures corroborated these findings, showing consistent behavior with temperature-variable experiments (Supplementary Figs. 43, 44)[32,33]. These results established a clear structure-property relationship for these atropisomers, where steric engineering controls the intensity and stability of TSC, enabling precise modulation of their luminescent wavelength.

Additionally, as described above, 22-NB adopts an averaged conformation while 11-NB-8DMe-*anti* maintains a single stable conformation. Both compounds exhibit nearly invariant emission profiles in temperature-dependent PL spectra (Fig. 2a, c), confirming that the spectral characteristics of emission in single-conformation systems remain thermally stable under temperature perturbation. Conversely, 11-NB shows temperature-dependent conformational populations (Fig. 1e, f), with synchronized PL emission shifts occurring over identical temperature ranges (Fig. 2b). This correlation establishes fluorescence as a sensitive probe for conformational dynamics.

Collectively, these findings demonstrate that PL spectroscopy has the potential to serve as an effective tool for quantifying atropisomer conformation populations—a principle substantiated in subsequent sections (Fluorescence mapping of atropisomer population and crystallization kinetics, Fig. 4).

To elucidate the origin of the observed photophysical difference in 22-NB, 11-NB and 11-NB-8DMe-*anti*, intramolecular interactions of their excited-state geometries using the independent gradient model based on Hirshfeld partitioning (IGMH) were performed (Fig. 2d)[34–36]. 22-NB shows a complete absence of intramolecular interactions and TSC, which is consistent with its temperature-independent and short-wavelength emission from isolated naphthalene. However, the IGMH surface of 11-NB (both *syn* and *anti* conformers) and 11-NB-8DMe-*anti* exhibit clear evidence of nonconvalent intramolecular interactions[37], which aligns closely with their redshifted emission from intramolecular TSC between two naphthalene units.

Accordingly, since 22-NB is identified as a Class 1 atropisomer under the LaPlente classification ($\Delta G < 84$ kJ/mol) with a low rotational barrier that permits unrestricted 360° rotation between its naphthalene and phenyl units[29], its pronounced flexibility markedly destabilizes the transient TSC (Fig. 2e). In contrast, 11-NB falls into Class 2 atropisomer (84 kJ/mol $< \Delta G <$ 117 kJ/mol), where slowed interconversion between *syn* and *anti* conformations enables temperature-responsive and switchable TSC. Further restricting molecular motion by methyl groups in 11-NB-8DMe-*anti* yields a rigid skeleton, facilitating the formation of exceptionally stable TSC[38]. Together, these results establish a direct correlation between single-molecule dynamics and electronic TSC in the solution state, providing critical mechanistic insights into the unexplored TSC behavior of atropisomers.

Separation and typical features of *syn* and *anti* conformers

Following the above principles for achieving conformer separation in atropisomeric systems, 11-NB-2DMe was precisely designed for isolating and studying its *syn* and *anti* conformers (Fig. 3a, Supplementary Figs. 6, 7). Compared to 11-NB-8DMe, the changed substitution positions of adjacent methyl groups decreases the steric hindrance of the *syn* conformer. As a result, 11-NB-2DMe satisfies the two essential criteria for realizing complete separation: (i) minimal free energy difference between conformers ($\Delta G_{syn\text{-}anti} = -2.8$ kJ/mol, Supplementary Fig. 38); (ii) slow interconversion kinetics, with $t_{1/2}$ of 4464 years for *syn* and 1442 years for *anti* conformer, respectively, qualifying it as Class 3 atropisomer ($\Delta G >$ 117 kJ/mol) under the LaPlente classification. Thus, the isolation of pure *syn* and *anti* conformers via fractional crystallization is successfully achieved. XRD, NMR, and HPLC analyses confirm the high purity and stereostructure of the obtained 11-NB-2DMe-*syn* and 11-NB-2DMe-*anti* conformers (Supplementary Figs. 18–21, 31). Photophysical studies reveal that while the *syn* and *anti* conformers exhibit nearly identical absorption spectra with characteristic peaks at 221 and 285 nm, their PL behavior differed (Fig. 3b, c). 11-NB-2DMe-*syn* displays dual emission, where the structured bands at 330 nm and 342 nm originate from the isolated naphthalene ring, and another broad long-wavelength peak around 372–383 nm is attributed to TSC. Upon cooling, the intensity of the TSC emission increases significantly due to the restricted intramolecular motions. Meanwhile, 11-NB-2DMe-*anti* exhibits dominant TSC emission at 378 nm, which is of significantly greater intensity than its residual naphthalene emission at 330 nm.

Although IGMH analysis reveals noncovalent interactions between the two naphthalene rings (green regions) in both 11-NB-2DMe-*syn* and 11-NB-2DMe-*anti*, the *anti* conformer exhibits more extensive interaction regions than its *syn* counterpart, consistent with the enhanced TSC emission observed in the PL spectra of the *anti* conformer (Fig. 3d, e). Furthermore, the reorganization energy (λ), which functions as a quantitative measure of inherent geometric changes upon photoexcitation and the contribution of intramolecular motion to non-radiative decay, was calculated[39]. For 11-NB-2DMe-*syn*, it exhibits a substantially high total λ of 6130 cm^{-1} compared to 11-NB-2DMe-*anti* of 3190 cm^{-1}. Notably, the dihedral angle torsional motions (yellow region), dominating the non-radiative relaxation process, contribute 63.85% and 51.41% to the total reorganization energy for the *syn* and *anti* conformers, respectively (Fig. 3f, g). Interestingly, 11-NB-2DMe-*syn* exhibits a pronounced butterfly-like swinging motion that substantially contributes to its larger λ (Supplementary Fig. 50), a feature absent in 11-NB-2DMe-*anti*. These results prove the flexible skeleton and strong intramolecular motions upon photoexcitation of the *syn* conformer, resulting in its unstable TSC and short-wavelength emission.

Unlike conventional H- and J-aggregates[40], the intramolecular dimers of naphthalene in 11-NB-2DMe preserve the ground-state electronic structure of isolated naphthalene (evidenced by unchanged absorption peaks) while significantly altering excited-state properties. Hole-electron analysis based on excited-state geometries confirms the presence of orbital overlap between naphthalene rings in both *syn* and *anti* conformers of 11-NB-2DMe (Supplementary Fig. 51)[41], indicating the existence of TSC. However, these conformers exhibit markedly different intensity ratios of emission from TBC and TSC, revealing the mutually competing radiative transition channels of TBC and TSC. Specifically, face-to-face H-dimer stacking suppresses the low-level radiative transition of TSC, whereas staggered J-dimer stacking enhances its radiative efficiency (Fig. 3h, i, Supplementary Fig. 52). Thus, the emission intensity ratios between TBC and TSC, which are strongly modulated by naphthalene stacking patterns, could be a potential ultra-sensitive approach for differentiating two conformers and even mapping their populations in complex environments.

Fluorescence mapping of atropisomer population and crystallization kinetics

For 11-NB-2DMe, the separation and purification of its *syn* and *anti* conformers pose significant challenges. Although fractional crystallization successfully achieves isolation of these conformers, the underlying crystallization kinetics remain poorly unexplored[42–45]. Direct mapping of conformers and thus visualizing the crystallization dynamics may provide mechanistic insights into atropisomeric formation and separation.

To verify the ability of fluorescence signals to differentiate atropisomeric conformers, the PL spectra of 11-NB-2DMe with varying *syn*/*anti* ratios is characterized (Fig. 4a). A near-perfect linear correlation ($R^2 = 0.9808$) between the relative PL intensity (I_{365}/I_{342}) and *syn*/*anti* ratio is observed, where I_{365} and I_{342} represent characteristic emission intensity of 11-NB-2DMe-*anti* (365 nm) and 11-NB-2DMe-*syn* (342 nm) conformers, respectively (Fig. 4d). This robust correlation ensures ratiometric fluorescence as a powerful real-time probe for mapping populations of atropisomeric conformers during crystallization processes. Hence, to qualitatively probe the crystallization kinetics, absorption spectra of 11-NB-2DMe-*syn* and 11-NB-2DMe-*anti* are acquired in dilute solutions across a concentration gradient (Fig. 4b, c). Both conformers exhibit strict adherence to the Lambert-Beer law ($R^2 > 0.99$) at 285 nm within the tested concentration range (Fig. 4e, f), validating absorbance spectroscopy as a quantitative method for determining solute concentrations during crystallization.

Based on the above results, the complete crystallization process of 11-NB-2DMe is further monitored in its entirety (Supplementary Fig. 53). Fluorescence analysis shows that the I_{365}/I_{342} ratio remains stable at ~0.69 during the initial phase (0–3 h). Subsequently, this ratio exhibits a progressive increase over time, reaching 1.06 at 24 h (Fig. 4g, Supplementary Table 4a, b). Combined with absorption measurements that reflect solution concentration, these optical analyses enable quantification of the real-time relative populations and mass for two specific conformers in solution. This integrated approach reveals three distinct kinetic stages throughout the crystallization process

https://doi.org/10.1038/s41467-026-69109-5

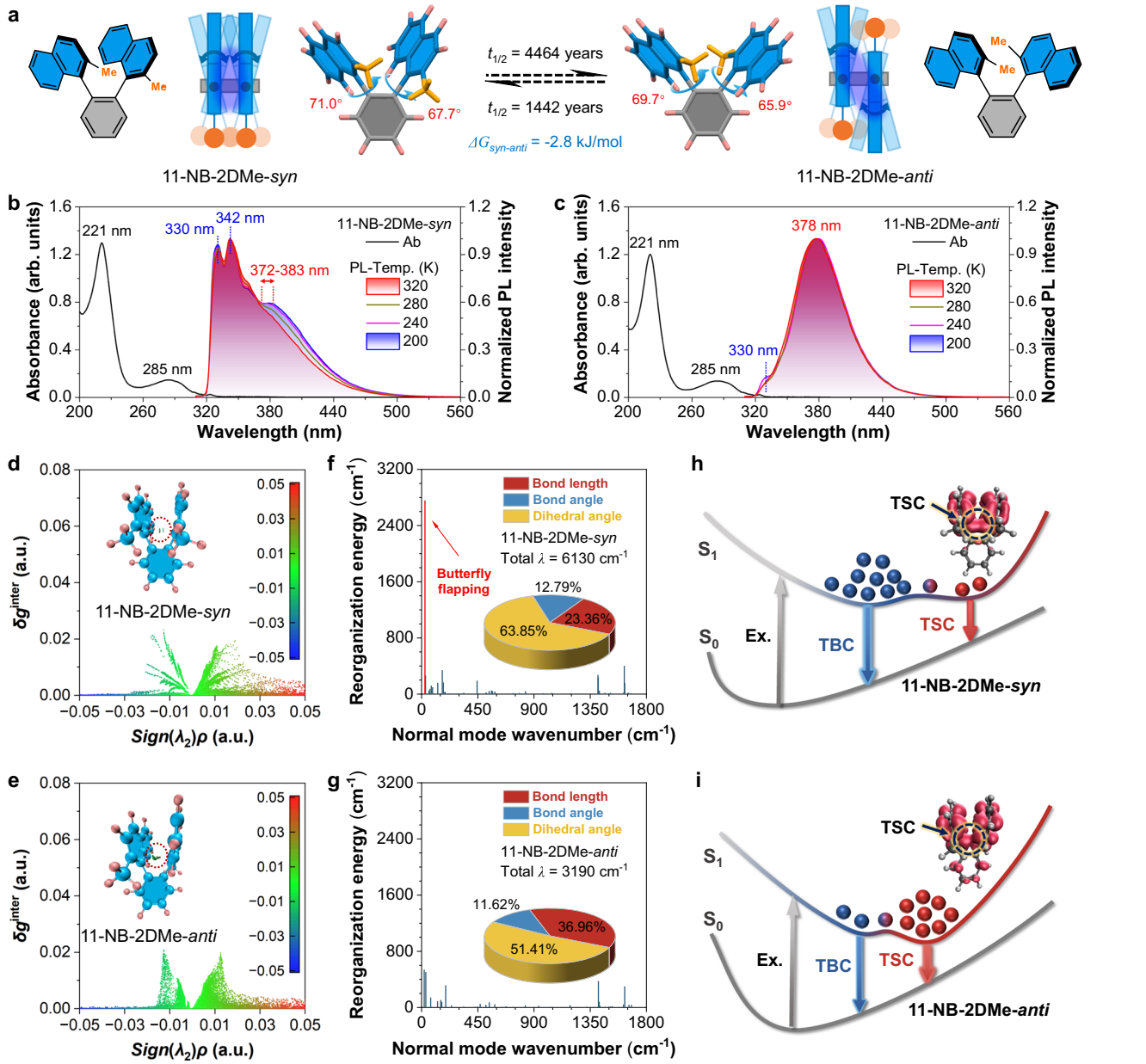

Fig. 3 | Separating and characterizing *syn* and *anti* conformers of 11-NB-2DMe. **a** Chemical structures, single-crystal structures, and calculated free energies and half-lives of 11-NB-2DMe. Absorbance and temperature-dependent PL spectra of **b** 11-NB-2DMe-*syn* and **c** 11-NB-2DMe-*anti* in 2-Me-THF, $c = 10$ μM. **d**, **e** Plots of δg^{inter} *versus* $sign(\lambda_2)\rho$. The inset displays the optimized excited-state geometry of 11-NB-2DMe, where interactions between its two naphthalene rings, analyzed by IGMH (isovalue = 0.018 a.u.), are circled by red dashed lines. **f**, **g** Plots of reorganization energy *versus* normal mode wavenumber of 11-NB-2DMe in the gas phase. Inset: Proportions of bond length, bond angle, and dihedral angle contributing to total reorganization energy. **h**, **i** Schematic diagram of the photophysics of 11-NB-2DMe atropisomers. Excited-state electronic structures are analyzed using the hole-electron method.

(Fig. 4h, i). (1) During the initial stage (0–3 h), the solution volume decreases without changes in conformer populations or total solute mass of 11-NB-2DMe-*syn* and 11-NB-2DMe-*anti*, indicating solvent evaporation leading to saturation prior to nucleation. (2) The second stage (3–21 h) displays a selective reduction in the *syn*-conformer population concurrent with accumulation of the *anti* conformer in solution, a dynamic driven solely by preferential crystallization of *syn* conformers. During this stage, the *syn*-nuclei formation and crystal growth generated harvestable high-purity 11-NB-2DMe-*syn* crystals. (3) Upon reaching the 21-hour mark, the third crystallization stage represents concurrent crystallization of both conformers until process completion, as evidenced by simultaneous mass reduction of their solutes. The third stage leads to mixed crystal growth, precluding high-purity isolation of 11-NB-2DMe-*anti* due to inseparable blending of *syn*- and *anti*-crystalline domains. Reproducibility was confirmed through replicate experiments (Supplementary Figs. 54, 55).

Throughout the sequential crystallization process from concentration (stage I), selective crystallization (stage II), and competitive crystallization (stage III), ratiometric fluorescence approach enables precise and real-time mapping of *syn*/*anti* conformer populations in 11-NB-2DMe (Fig. 4j). This non-destructive nature and molecular-level sensitivity of fluorescence mapping provides complete visualization of crystallization kinetics, establishing it as a powerful tool for mapping complex crystallization processes in atropisomeric systems.

https://doi.org/10.1038/s41467-026-69109-5

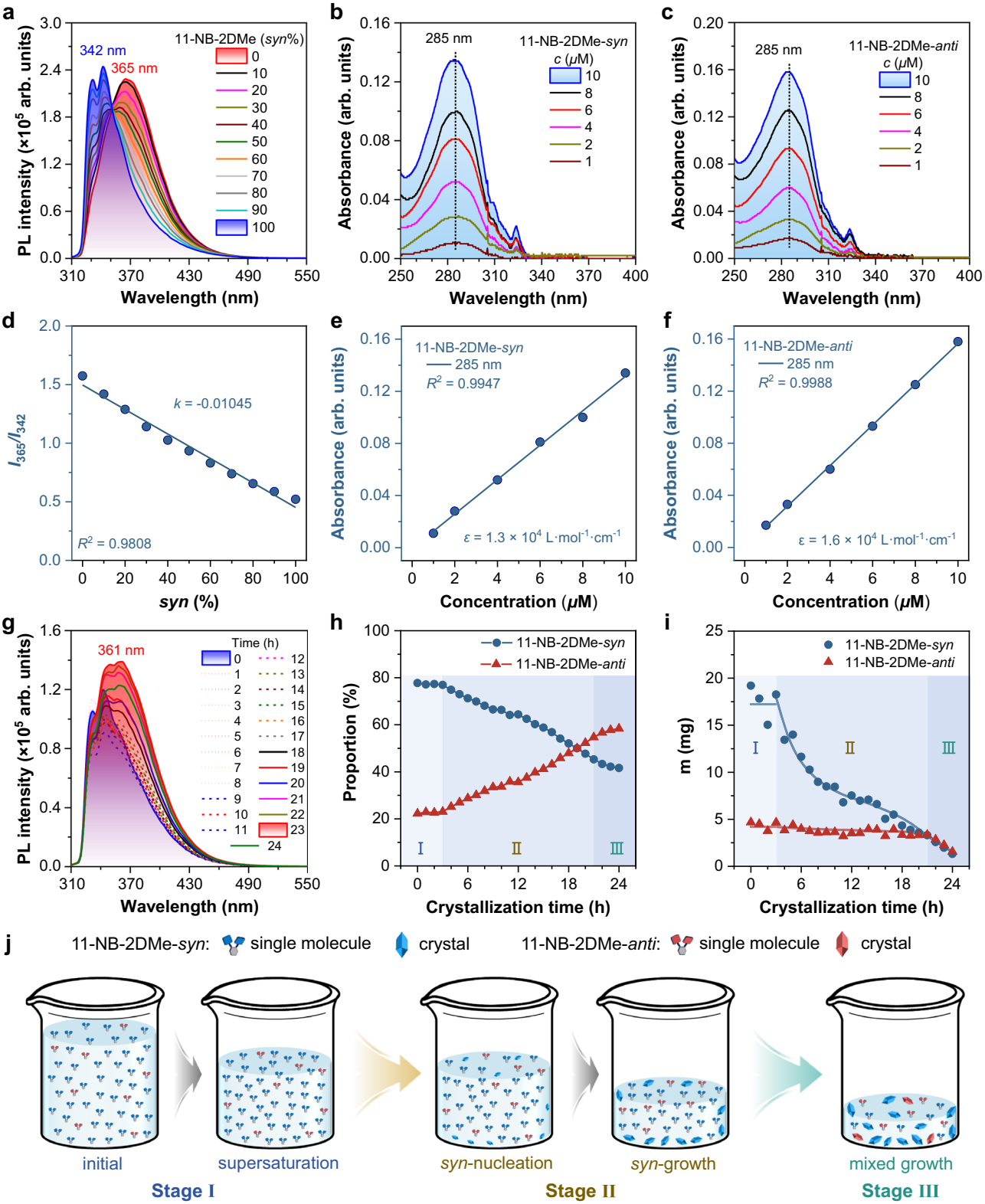

Fig. 4 | Visualizing crystallization kinetics of 11-NB-2DMe. a PL spectra of 11-NB-2DMe in acetonitrile (ACN) with varying *syn* and *anti* fractions, $c = 10$ μM. Absorption spectra of **b** 11-NB-2DMe-*syn* and **c** 11-NB-2DMe-*anti* in ACN with different concentrations. **d** Plot of relative PL intensity (I_{365}/I_{342}) *versus syn* fraction in panel (**a**). Plots of absorbance of **e** 11-NB-2DMe-*syn* and **f** 11-NB-2DMe-*anti* at 285 nm *versus* concentration in panels (**b**, **c**). **g** PL spectra of 11-NB-2DMe during its crystallization in ACN at various crystallization times. Plots of **h** population ratios and **i** mass (m) of *syn* and *anti* conformers during the crystallization. **j** Schematic diagram of three stages of 11-NB-2DMe crystallization.

Therefore, this study successfully constructs and characterizes a series of biaxial atropisomers using naphthalene rotors and phenyl linkers, focusing on their complex stereoconformations and dynamic interconversion mechanisms. Through precise structural modulation, three LaPlente-type atropisomers are synthesized with tailored thermodynamic and kinetic properties. The correlation between molecular dynamics and TSC is elucidated, demonstrating that TSC-induced fluorescence variations enable real-time mapping of atropisomer populations. Notably, the *syn* and *anti* conformers of 11-NB-2DMe are completely separated and characterized. Fluorescence mapping provides insights into the dynamic conformational population during crystallization, revealing temporally sequential crystallization where *syn* conformers undergo preferential nucleation during the initial stage, while *anti* conformers exhibit delayed crystallization behavior. This work significantly advances atropisomer science by establishing a fluorescence-enabled in-situ platform for real-time mapping of atropisomeric dynamics, thereby deepening fundamental stereochemical theory and opening possibilities for studying molecular dynamics in diverse matter and biological systems.

Methods

Materials

All reagents were purchased from commercial suppliers (Leyan, Energy Chemical, Macklin, Aladdin, J&K Scientific, or Bidepharm) and used without further purification. Specifically, tetrakis(triphenylphosphine)palladium was obtained from Leyan (Cat No.1021232, Leyan, Shanghai, China). All the final products used in experiments were purified through a silica gel column and recrystallization at least three times. Purification of all samples was checked by high-performance liquid chromatography (HPLC). HPLC-grade acetonitrile (ACN), toluene (Tol), and 2-methyltetrahydrofuran (2-Me-THF) were used for synthesis and photophysical measurements.

Instrumentation and analytical techniques

^{1}H and ^{13}C NMR spectra were recorded on Bruker AVANCE NEO 400 MHz and 500 MHz spectrometers. Deuterated solvents, including CD_2Cl_2, THF-d_8, CD_3CN, DMSO-d_6, and $CDCl_3$, were used without further purification. Variable-temperature ^{1}H NMR spectra were acquired on a Bruker AVANCE NEO 600 MHz instrument. UV-Vis absorption spectra were measured using a Shimadzu UV-2600 spectrophotometer. Photoluminescence spectra, absolute fluorescence quantum yields, and fluorescence lifetimes were obtained on a Shimadzu RF-6000 spectrofluorophotometer coupled with an Edinburgh Instruments FLS1000 spectrometer. Single crystals of the target compounds were mounted directly on a Bruker D8 Venture diffractometer. Data collection was performed at 250.00 K. Structures were solved using ShelXT 2018/2 (dual-space algorithm) and refined with ShelXL 2019/2 (full-matrix least-squares on F^2) via the Olex2 1.5 interface. HPLC measurements were conducted on a Waters 2690 separations module with a C18 reverse-phase column. High-resolution mass spectra of these compounds were all obtained through fourier transform mass spectrometry (FTMS), and test instrument is Thermo Scientific Exactive GC Orbitrap (Thermo Scientific).

Computational details

All the compounds were fully optimized with the density functional theory (DFT) method by using the B3LYP density functional and 6−31 G(d,p) basis set[46] London-dispersion effects were also taken into consideration using Grimme's DFT-D3BJ correction[47,48] Analytical frequency calculations were also performed at the same level of theory to confirm that the optimized structures were at a minimum point. Time-dependent density functional theory (TD-DFT)[49] was utilized at the same level of theory to calculate optimized excited singlet-state (S_1) geometries and energy levels. All the above quantum chemical calculations were carried out using the Gaussian 16 program[50]. Shermo was employed to calculate Gibbs free energy extraction from Gaussian-derived checkpoint files (.fchk), applying ZPVE scaling (factor = 0.9806) at 298 K[51]. The Eyring equation

$$k = \kappa \frac{k_B T}{h} e^{-\frac{\Delta G^{\neq}}{RT}}$$

defines the reaction rate constant k through transition state theory, where κ is the transmission coefficient (typically unity), k_B is the Boltzmann constant, T is the absolute temperature in Kelvin (298 K in this work), h is the Planck's constant, $\Delta G^{\neq}$ is the Gibbs free energy of activation in kJ/mol, and R is the universal gas constant. For first-order reactions, the half-life follows as

$$t_{1/2} = \ln(2)/k$$

Reorganization energy analysis based on normal-mode-projected displacements and Duschinsky rotation matrices under curvilinear coordinates was performed using the Molecular Materials Property Prediction Package (MOMAP) based on the formatted checkpoint file (.fchk) obtained from Gaussian[39,52,53]. IGMH analyses[34] were calculated by Multiwfn 3.8[35], and were displayed using Visual Molecular Dynamics (VMD)[54] (Isovalue: 0.018). Hole-electron analyses[41] were calculated by Multiwfn 3.8, and were displayed using IQmol molecular viewer package (Isovalue: 0.001).

Data availability

The crystallographic data for the structures reported in this article have been deposited at the Cambridge Crystallographic Data Centre (CCDC) under deposition numbers 2470573 (22-NB), 2470574 (11-NB), 2470575 (111-NB), 2470576 (11-NB-8DMe), 2470577 (11-NB-2DMe-*syn*), 2470578 (11-NB-2DMe-*anti*). These data can be obtained free of charge from CCDC via www.ccdc.cam.ac.uk/data_request/cif. All the data supporting the findings in this work are available within the manuscript and Supplementary Information file and available from the corresponding authors upon request.

References

1. Kozlowski, M. C., Miller, S. J. & Perreault, S. Atropisomers: synthesis, analysis, and applications. *Acc. Chem. Res.* **56**, 187–188 (2023).
2. Perreault, S., Chandrasekhar, J. & Patel, L. Atropisomerism in drug discovery: a medicinal chemistry perspective inspired by atropisomeric class I PI3K inhibitors. *Acc. Chem. Res.* **55**, 2581–2593 (2022).
3. Clayden, J., Moran, W. J., Edwards, P. J. & LaPlante, S. R. The challenge of atropisomerism in drug discovery. *Angew. Chem. Int. Ed.* **48**, 6398–6401 (2009).
4. Barrett, K. T., Metrano, A. J., Rablen, P. R. & Miller, S. J. Spontaneous transfer of chirality in an atropisomerically enriched two-axis system. *Nature* **509**, 71–75 (2014).
5. Xiang, S.-H., Ding, W.-Y., Wang, Y.-B. & Tan, B. Catalytic atroposelective synthesis. *Nat. Catal.* **7**, 483–498 (2024).
6. Collins, B. S. L., Kistemaker, J. C. M., Otten, E. & Feringa, B. L. A chemically powered unidirectional rotary molecular motor based on a palladium redox cycle. *Nat. Chem.* **8**, 860–866 (2016).
7. Berreur, J. et al. Redox-powered autonomous directional C-C bond rotation under enzyme control. *Nature* **644**, 96–101 (2025).
8. Wang, M. et al. Asymmetric hydrogenation of ketimines with minimally different alkyl groups. *Nature* **631**, 556–562 (2024).
9. Ren, Y., Jamagne, R., Tetlow, D. J. & Leigh, D. A. A tape-reading molecular ratchet. *Nature* **612**, 78–82 (2022).
10. Qi, L.-W., Li, S., Xiang, S.-H., Wang, J. & Tan, B. Asymmetric construction of atropisomeric biaryls via a redox neutral cross-coupling strategy. *Nat. Catal.* **2**, 314–323 (2019).

11. Gustafson, J. L. et al. Dynamic kinetic resolution of biaryl atropisomers via peptide-catalyzed asymmetric bromination. *Science* **328**, 1251–1255 (2010).
12. Wencel-Delord, J., Panossian, A., Leroux, F. R. & Colobert, F. Recent advances and new concepts for the synthesis of axially stereoenriched biaryls. *Chem. Soc. Rev.* **44**, 3418–3430 (2015).
13. Abe, S., Kikuchi, J., Matsumoto, A. & Yoshikai, N. Stable and responsive atropisomerism around a carbon–iodine bond. *Chem* **11**, 102527 (2025).
14. Wu, X. et al. Catalyst control over sixfold stereogenicity. *Nat. Catal.* **4**, 457–462 (2021).
15. Wu, F., Zhang, Y., Zhu, R. & Huang, Y. Discovery and synthesis of atropisomerically chiral acyl-substituted stable vinyl sulfoxonium ylides. *Nat. Chem.* **16**, 132–139 (2024).
16. Simek, M. et al. Nucleophilic aromatic substitutions enable diversity-oriented synthesis of heterocyclic atropisomers via non-atropisomeric intermediates. *Nat. Commun.* **16**, 4856 (2025).
17. Schmidt, T. A., Hutskalova, V. & Sparr, C. Atroposelective catalysis. *Nat. Rev. Chem.* **8**, 497–517 (2024).
18. Nagami, S. et al. Photoinduced dual bond rotation of a nitrogen-containing system realized by chalcogen substitution. *Nat. Chem.* **16**, 959–969 (2024).
19. Bismillah, A. N. et al. Control of dynamic sp^3-C stereochemistry. *Nat. Chem.* **15**, 615–624 (2023).
20. Saha, P. K. et al. Rupturing aromaticity by periphery overcrowding. *Nat. Chem.* **15**, 516–525 (2023).
21. Kang, C. et al. Covalent organic framework atropisomers with multiple gas-triggered structural flexibilities. *Nat. Mater.* **22**, 636–643 (2023).
22. Oguadinma, P., Bilodeau, F. & LaPlante, S. R. NMR strategies to support medicinal chemistry workflows for primary structure determination. *Bioorg. Med. Chem. Lett.* **27**, 242–247 (2017).
23. Shen, P. et al. Switchable dual circularly polarized luminescence in through-space conjugated chiral foldamers. *Angew. Chem. Int. Ed.* **63**, e202407605 (2024).
24. Liu, J. et al. Through-space interaction of tetraphenylethylene: what, where, and how. *J. Am. Chem. Soc.* **144**, 7901–7910 (2022).
25. Zhang, J. et al. How to manipulate through-space conjugation and clusteroluminescence of simple aiegens with isolated phenyl rings. *J. Am. Chem. Soc.* **143**, 9565–9574 (2021).
26. Han, Y.-Q. et al. Fjord-type AIEgens based on inherent through-space conjugation. *CCS Chem* **6**, 1739–1747 (2024).
27. Wang, Y. et al. Narrowband clusteroluminescence with 100% quantum yield enabled by through-space conjugation of asymmetric conformation. *Nat. Commun.* **15**, 6426 (2024).
28. Canfield, P. J. et al. A new fundamental type of conformational isomerism. *Nat. Chem.* **10**, 615–624 (2018).
29. Heeb, J. P., Clayden, J., Smith, M. D. & Armstrong, R. J. Interrogating the configurational stability of atropisomers. *Nat. Protoc.* **18**, 2745–2771 (2023).
30. Tu, W. et al. The superiority of nonconjugated structures in fluorescence: through-space vs. through-bond charge transfer. *Sci. China Chem.* **67**, 3121–3130 (2024).
31. Xu, J. et al. π-Bridge mediated coupling between inter- and intramolecular charge transfer in aggregates for highly efficient near-infrared emission. *Aggregate* **5**, e634 (2024).
32. Xu, Q., Zhang, J., Sun, J. Z., Zhang, H. & Tang, B. Z. Efficient organic emitters enabled by ultrastrong through-space conjugation. *Nat. Photon.* **18**, 1185–1194 (2024).
33. Zhang, J., Xiong, Z., Zhang, H. & Tang, B. Z. Emergent clusteroluminescence from nonemissive molecules. *Nat. Commun.* **16**, 3910 (2025).
34. Lu, T. & Chen, Q. Independent gradient model based on Hirshfeld partition: a new method for visual study of interactions in chemical systems. *J. Comput. Chem.* **43**, 539–555 (2022).
35. Lu, T. & Chen, F. Multiwfn: a multifunctional wavefunction analyzer. *J. Comput. Chem.* **33**, 580–592 (2012).
36. Lu, T. A comprehensive electron wavefunction analysis toolbox for chemists, Multiwfn. *J. Chem. Phys.* **161**, 082503 (2024).
37. Liu, C. et al. Intermolecular through-space charge transfer enabled by bicomponent assembly for ultrasensitive detection of synthetic cannabinoid JWH-018. *Aggregate* **4**, e315 (2023).
38. Tu, W. et al. Manipulation of the through-space interactions in diphenylmethane. *Smart Mol* **1**, e20220006 (2023).
39. Shuai, Z. & Peng, Q. Organic light-emitting diodes: theoretical understanding of highly efficient materials and development of computational methodology. *Natl. Sci. Rev.* **4**, 224–239 (2017).
40. Xu, J. et al. C—H···π interaction induced H-aggregates for wide range water content detection in organic solvents. *Aggregate* **5**, e546 (2024).
41. Liu, Z., Lu, T. & Chen, Q. An sp-hybridized all-carboatomic ring, cyclo[18]carbon: Electronic structure, electronic spectrum, and optical nonlinearity. *Carbon* **165**, 461–467 (2020).
42. Chen, M. et al. Enabling polymer single crystals to be high-performance dielectric. *Angew. Chem. Int. Ed.* **63**, e202314685 (2024).
43. Yang, Y., Chen, M., Li, H. & Li, H. The degree of crystallinity exhibiting a spatial distribution in polymer films. *Eur. Polym. J.* **107**, 303–307 (2018).
44. Hou, I., Li, L., Zhang, H. & Naumov, P. Smart molecular crystal switches. *Smart Mol.* **2**, e20230031 (2024).
45. Lu, S., Chen, M. & Li, H. Nucleation site memory in the spherulite films of polydisperse poly(L-lactic acid). *Macromolecules* **57**, 10219–10226 (2024).
46. Tirado-Rives, J. & Jorgensen, W. L. Performance of B3LYP density functional methods for a large set of organic molecules. *J. Chem. Theory Comput.* **4**, 297–306 (2008).
47. Goerigk, L. A comprehensive overview of the DFT-D3 London-dispersion correction. In *Non-Covalent Interactions in Quantum Chemistry and Physics: Theory and Applications* (eds Otero de la Roza, A. et al.) 195–219 (Elsevier, 2017).
48. Cukras, J. & Sadlej, J. The influence of the dispersion corrections on the performance of DFT method in modeling HNgY noble gas molecules and their complexes. *Chem. Phys. Lett.* **691**, 319–324 (2018).
49. Adamo, C. & Jacquemin, D. The calculations of excited-state properties with time-dependent density functional theory. *Chem. Soc. Rev.* **42**, 845–856 (2013).
50. Frisch, M. J. et al. Gaussian. Revision A 16, 03 (2017).
51. Lu, T. & Chen, Q. Shermo: a general code for calculating molecular thermochemistry properties. *Comput. Theor. Chem.* **1200**, 113249 (2021).
52. Shuai, Z. & Peng, Q. Excited states structure and processes: understanding organic light-emitting diodes at the molecular level. *Phys. Rep.* **537**, 123–156 (2014).
53. Reimers, J. R. A practical method for the use of curvilinear coordinates in calculations of normal-mode-projected displacements and Duschinsky rotation matrices for large molecules. *J. Chem. Phys.* **115**, 9103–9109 (2001).
54. Humphrey, W., Dalke, A. & Schulten, K. VMD: visual molecular dynamics. *J. Mol. Graph.* **14**, 33–38 (1996).

Acknowledgements

This work is supported by the National Natural Science Foundation of China (No. 224B2509, received by Q.X.; No. 22575211, received by H.Z.; No. 524B2036, received by Z.X.; No. 52503253, received by J.Z.), the Fundamental Research Funds for the Central Universities (No. 226-2025-00031, received by H.Z.; No. 226-2025-00091, received by J.Z.), the Open Fund of the State Key Laboratory of Luminescent Materials and Devices (South China University of Technology, received by H.Z.), Seed

Program of China Petroleum & Chemical Corporation (Sinopec, received by H.Z.), the Large Instruments Open Foundation of Nantong University (KFJN2551, received by Y.W.). We thank Yingying Zhang from the Testing and Analysis Center of the Department of Polymer Science and Engineering at Zhejiang University for the assistance in performing Photoluminescence Spectroscopy measurements. We thank Jiyong Liu from the Testing and Analysis Center of the Department of Chemistry at Zhejiang University for the help in performing X-ray single crystal diffractometer measurements. We thank the Guangdong Provincial Key Laboratory of Luminescence from Molecular Aggregates for the help in quantum mechanical calculations.

Author contributions

Q.X., J.Z., and H.Z. conceived and designed the experiments. Q.X., and K.L. performed the synthesis and the photophysical measurements. Q.X. conducted theoretical calculations. J.W., H.L., M.C., and Z.X. provided significant assistance with the experimental measurements. Q.X., J.Z., and H.Z. analyzed the data. Q.X., Y.W., J.Z.S, J.Z., F.H., B.Z.T., and H.Z. took part in the discussion and gave important suggestions. Q.X., J.Z., and H.Z. co-wrote the paper.

Competing interests

The authors declare no competing interests.

Additional information

Supplementary information The online version contains supplementary material available at https://doi.org/10.1038/s41467-026-69109-5.

Correspondence and requests for materials should be addressed to Jianyu Zhang, Feihe Huang, Ben Zhong Tang or Haoke Zhang.

Peer review information *Nature Communications* thanks the anonymous reviewers for their contribution to the peer review of this work. A peer review file is available.